Antiproton Flux, Antiproton-to-Proton Flux Ratio, and Properties of Elementary Particle Fluxes in Primary Cosmic Rays Measured with the Alpha Magnetic Spectrometer on the International Space Station
SUPPLEMENTAL MATERIAL

(AMS Collaboration)

For references see the main text.

Detector.— The layout and description of the AMS detector are presented in Ref. [17]. The cross section of the detector is shown in Fig. SM 1. All detector elements are used in the present analysis including the precision silicon tracker [19], the permanent magnet [5, 20], the four planes of time of flight counters TOF [21], the array of anti-coincidence counters ACC [22], the transition radiation detector TRD [23], the ring imaging Čerenkov detector RICH [24], and the electromagnetic calorimeter ECAL [25]. The AMS coordinate system is concentric and coaxial with the magnet. The x axis is parallel to the main component of the magnetic field and the z axis points vertically. The $(y$–$z)$ plane is the bending plane.

Together, the tracker and the magnet measure the rigidity $R = pc/Ze$ of charged cosmic rays with momentum p and charge Z. The tracker has nine layers, the first (L1) at the top of the detector, the second (L2) just above the magnet, six (L3 to L8) within the bore of the magnet, and the last (L9) just above the ECAL. L2 to L8 constitute the inner tracker. Each layer contains double-sided silicon microstrip detectors that independently measure the x and y coordinates. The tracker accurately determines the particle trajectory by multiple measurements of the coordinates with a resolution in each layer of 10 μm in the bending (y) direction. The inner tracker is held stable by a carbon fiber structure with negligible coefficient of thermal expansion. The stability of the inner tracker is monitored using 20 IR laser beams that penetrate layers L2 through L8 and provide submicron position measurements. Using cosmic rays over a 2 minute window, the position of L1 is aligned with a precision of 5 μm with respect to the inner tracker and L9 with a precision of 6 μm. The maximum detectable rigidity, MDR, is 2 TV over the 3 m lever arm from L1 to L9 for $|Z| = 1$. Each layer of the tracker also provides an independent measurement of $|Z|$. The charge resolution of the layers of the inner tracker together is $\Delta Z = 0.05$ for $|Z| = 1$.

The TOF counters measure the velocity $\beta = v/c$ and $|Z|$ of cosmic rays. Two TOF planes are located above L2 and two planes are located below the magnet. For $|Z| = 1$ particles, the average time resolution of each counter is 160 ps and the overall velocity $(\beta = v/c)$ resolution $\Delta\beta/\beta^2 = 4\%$. This discriminates between downward- and upward-going particles. The coincidence of signals from the four TOF planes together with the absence of coincident signals from the ACC provides a $|Z| = 1$ trigger. The ACC has a measured efficiency of 0.99999 to reject cosmic rays which enter the inner tracker from the side. The coincidence of 3 out of the 4 TOF layers with no ACC requirement provides an unbiased trigger. The unbiased trigger, prescaled to 1%, is used to measure the efficiency of the $|Z| = 1$ trigger.

The TRD uses transition radiation to distinguish $\bar{p}$ and p from e^- and e^+. It consists of 5248 proportional tubes of 6 mm diameter with a maximum length of 2 m assembled in 16-tube modules. The 328 modules are mounted in 20 layers. There are 12 layers of proportional tubes along the y axis located in the middle of the TRD and, along the x axis, four layers located on top and four on the bottom.

The ring imaging Čerenkov detector measures velocity and $|Z|$. In the present analysis this allows the separation of $\bar{p}$ from light particles (e^- and π^-). It consists of two radiators, an expansion volume, and a photodetection plane. The dielectric radiators induce the emission of a cone of Čerenkov photons when traversed by charged particles with a velocity greater than the velocity of light in the material, $\beta > 1/n$ where n is the refractive index. The central radiator is formed by 16 sodium fluoride, NaF, tiles, each $85 \times 85 \times 5$ mm^3, with $n = 1.33$. These are surrounded by 92 tiles, each $115 \times 115 \times 25$ mm^3, of silica aerogel with $n = 1.05$. This allows the detection of particles with velocities $\beta > 0.75$ with the NaF

radiator and $\beta > 0.953$ with the aerogel radiator. The expansion volume has a distance along z of 470 mm and is surrounded by a high reflectivity mirror to increase detection efficiency. The photodetection plane is an array of 10 880 photosensors with an effective spatial granularity of 8.5×8.5 mm^2. The sum of the signal amplitudes is proportional to Z^2. The opening angle of the Čerenkov radiation cone is a measure of the velocity of the incoming charged particle. Typical velocity resolution is $\Delta\beta/\beta = 0.1\%$ for $|Z| = 1$.

The three-dimensional imaging capability of the 17 radiation length ECAL allows for an accurate measurement of the $e^\pm$ energy E and shower shape. The energy resolution is $\sigma(E)/E = \sqrt{(0.104)^2/E + (0.014)^2}$ (E in GeV). The uncertainty of the absolute $e^\pm$ energy scale has been verified to be 2% in the range 10–290 GeV. Below 10 GeV it increases to 5% at 0.5 GeV and above 290 GeV to 4% at 700 GeV. The shower shape is used for the efficient separation of $\bar{p}$ and p from e^- and e^+ when the event enters the ECAL.

Figure SM 1 also shows the reconstruction of an antiproton event. The reconstructed trajectory, or track, is shown by the red line. The insets show zoomed views of the matching between this track and the pulse heights measured in each tracker layer. This downward-going $|Z| = 1$ event is identified as an antiproton with $R = -435$ GV, $\Lambda_{\mathrm{TRD}} = 0.908$, and $\Lambda_{\mathrm{CC}} = 0.983$.

Before launch, AMS was extensively calibrated at the CERN SPS with 180 and 400 GeV/c proton beams and positron, electron, and pion beams of 10 to 290 GeV/c. In total, calibrations with 18 different energies and particles at 2000 positions were performed. These data allow the determination of the tracker rigidity resolution function with high precision and the verification of the absolute rigidity scale. Since launch, the detector has been monitored and controlled around the clock. The time, location, and orientation are provided by GPS units affixed to AMS and to the ISS. The detector performance has been steady over time.

Simulated events were produced using a dedicated program developed by the collaboration from the GEANT 4.10.1 package [30] based on Monte Carlo methods. This program simulates electromagnetic and hadronic interactions of particles in the material of AMS and generates detector responses. The digitization of the signals is simulated precisely according to the measured characteristics of the electronics. The simulated events then undergo the same reconstruction as used for the data.

TABLE SM I: The $\bar{p}$ flux $\Phi^{\bar{p}}$ in units of $[\mathrm{m^2\,sr\,s\,GV}]^{-1}$ and the $(\bar{p}/p)$ flux ratio $\Phi^{\bar{p}}/\Phi^p$ as a function of absolute rigidity at the top of AMS. $\tilde{N}^{\bar{p}}$ is the number of antiprotons observed in each rigidity bin rounded to the nearest integer. σ_{stat} and σ_{syst} are the respective statistical and systematic errors.

Rigidity [GV]	$\tilde{N}^{\bar{p}}$	$\Phi^{\bar{p}}$ $\quad\sigma_{\mathrm{stat}}\;\sigma_{\mathrm{syst}}$	$\Phi^{\bar{p}}/\Phi^p$ $\quad\sigma_{\mathrm{stat}}\;\sigma_{\mathrm{syst}}$
$1.00 - 1.16$	21	$(5.94\ 1.31\ 0.58)\times10^{-3}$	$(1.02\ \ 0.23\ 0.08)\times10^{-5}$
$1.16 - 1.33$	74	$(5.57\ 0.68\ 0.51)\times10^{-3}$	$(8.93\ \ 1.09\ 0.66)\times10^{-6}$
$1.33 - 1.51$	233	$(9.75\ 0.68\ 0.68)\times10^{-3}$	$(1.59\ \ 0.11\ 0.09)\times10^{-5}$
$1.51 - 1.71$	502	$(1.06\ 0.05\ 0.07)\times10^{-2}$	$(1.83\ \ 0.09\ 0.09)\times10^{-5}$
$1.71 - 1.92$	888	$(1.25\ 0.05\ 0.08)\times10^{-2}$	$(2.33\ \ 0.10\ 0.12)\times10^{-5}$
$1.92 - 2.15$	1449	$(1.40\ 0.05\ 0.08)\times10^{-2}$	$(2.90\ \ 0.10\ 0.14)\times10^{-5}$
$2.15 - 2.40$	2192	$(1.50\ 0.05\ 0.09)\times10^{-2}$	$(3.50\ \ 0.11\ 0.17)\times10^{-5}$
$2.40 - 2.67$	3366	$(1.64\ 0.04\ 0.09)\times10^{-2}$	$(4.36\ \ 0.11\ 0.20)\times10^{-5}$
$2.67 - 2.97$	4474	$(1.64\ 0.04\ 0.09)\times10^{-2}$	$(5.05\ \ 0.12\ 0.23)\times10^{-5}$
$2.97 - 3.29$	6028	$(1.69\ 0.04\ 0.09)\times10^{-2}$	$(6.07\ \ 0.13\ 0.27)\times10^{-5}$
$3.29 - 3.64$	7321	$(1.67\ 0.03\ 0.09)\times10^{-2}$	$(7.05\ \ 0.14\ 0.30)\times10^{-5}$
$3.64 - 4.02$	8592	$(1.59\ 0.03\ 0.08)\times10^{-2}$	$(7.96\ \ 0.15\ 0.32)\times10^{-5}$
$4.02 - 4.43$	1932	$(1.56\ 0.04\ 0.08)\times10^{-2}$	$(9.31\ \ 0.21\ 0.37)\times10^{-5}$
$4.43 - 4.88$	3083	$(1.43\ 0.03\ 0.07)\times10^{-2}$	$(1.03\ \ 0.02\ 0.04)\times10^{-4}$
$4.88 - 5.37$	3880	$(1.23\ 0.02\ 0.06)\times10^{-2}$	$(1.07\ \ 0.02\ 0.04)\times10^{-4}$
$5.37 - 5.90$	4780	$(1.12\ 0.02\ 0.05)\times10^{-2}$	$(1.19\ \ 0.02\ 0.05)\times10^{-4}$
$5.90 - 6.47$	5472	$(9.80\ 0.13\ 0.45)\times10^{-3}$	$(1.27\ \ 0.02\ 0.05)\times10^{-4}$
$6.47 - 7.09$	6538	$(8.69\ 0.11\ 0.39)\times10^{-3}$	$(1.38\ \ 0.02\ 0.05)\times10^{-4}$
$7.09 - 7.76$	7369	$(7.59\ 0.09\ 0.34)\times10^{-3}$	$(1.49\ \ 0.02\ 0.05)\times10^{-4}$
$7.76 - 8.48$	7818	$(6.54\ 0.08\ 0.29)\times10^{-3}$	$(1.59\ \ 0.02\ 0.06)\times10^{-4}$
$8.48 - 9.26$	7821	$(5.46\ 0.06\ 0.24)\times10^{-3}$	$(1.64\ \ 0.02\ 0.06)\times10^{-4}$
$9.26 - 10.1$	20382	$(4.67\ 0.03\ 0.20)\times10^{-3}$	$(1.74\ \ 0.01\ 0.06)\times10^{-4}$
$10.1 - 11.0$	19445	$(3.96\ 0.03\ 0.17)\times10^{-3}$	$(1.83\ \ 0.01\ 0.07)\times10^{-4}$
$11.0 - 12.0$	18769	$(3.23\ 0.02\ 0.14)\times10^{-3}$	$(1.86\ \ 0.01\ 0.07)\times10^{-4}$
$12.0 - 13.0$	16372	$(2.65\ 0.02\ 0.11)\times10^{-3}$	$(1.89\ \ 0.02\ 0.07)\times10^{-4}$
$13.0 - 14.1$	16076	$(2.23\ 0.02\ 0.09)\times10^{-3}$	$(1.96\ \ 0.02\ 0.07)\times10^{-4}$
$14.1 - 15.3$	15578	$(1.85\ 0.02\ 0.08)\times10^{-3}$	$(2.02\ \ 0.02\ 0.07)\times10^{-4}$
$15.3 - 16.6$	14734	$(1.49\ 0.01\ 0.06)\times10^{-3}$	$(2.02\ \ 0.02\ 0.07)\times10^{-4}$
$16.6 - 18.0$	15816	$(1.19\ 0.01\ 0.05)\times10^{-3}$	$(2.00\ \ 0.02\ 0.07)\times10^{-4}$
$18.0 - 19.5$	15049	$(9.53\ 0.08\ 0.37)\times10^{-4}$	$(1.99\ \ 0.02\ 0.06)\times10^{-4}$
$19.5 - 21.1$	14426	$(7.72\ 0.07\ 0.29)\times10^{-4}$	$(1.99\ \ 0.02\ 0.06)\times10^{-4}$
$21.1 - 22.8$	13511	$(6.33\ 0.06\ 0.23)\times10^{-4}$	$(2.02\ \ 0.02\ 0.06)\times10^{-4}$
$22.8 - 24.7$	12943	$(5.02\ 0.05\ 0.18)\times10^{-4}$	$(1.99\ \ 0.02\ 0.06)\times10^{-4}$
$24.7 - 26.7$	11723	$(4.11\ 0.04\ 0.14)\times10^{-4}$	$(2.02\ \ 0.02\ 0.05)\times10^{-4}$
$26.7 - 28.8$	10411	$(3.32\ 0.04\ 0.11)\times10^{-4}$	$(2.02\ \ 0.02\ 0.05)\times10^{-4}$
$28.8 - 31.1$	9508	$(2.68\ 0.03\ 0.08)\times10^{-4}$	$(2.02\ \ 0.02\ 0.05)\times10^{-4}$
$31.1 - 33.5$	7876	$(2.07\ 0.03\ 0.06)\times10^{-4}$	$(1.92\ \ 0.02\ 0.04)\times10^{-4}$
$33.5 - 36.1$	7212	$(1.75\ 0.02\ 0.05)\times10^{-4}$	$(2.00\ \ 0.03\ 0.05)\times10^{-4}$

(Table continued)

TABLE SM I. *(Continued).*

Rigidity [GV]	$\tilde{N}^{\bar{p}}$	$\Phi^{\bar{p}}$ σ_{stat} σ_{syst}	$\Phi^{\bar{p}}/\Phi^{p}$ σ_{stat} σ_{syst}
$36.1 - 38.9$	6127	$(1.40\ 0.02\ 0.04)\times10^{-4}$	$(1.98\ \ 0.03\ 0.05)\times10^{-4}$
$38.9 - 41.9$	2697	$(1.10\ 0.02\ 0.03)\times10^{-4}$	$(1.92\ \ 0.04\ 0.05)\times10^{-4}$
$41.9 - 45.1$	2353	$(8.78\ 0.20\ 0.26)\times10^{-5}$	$(1.88\ \ 0.04\ 0.05)\times10^{-4}$
$45.1 - 48.5$	1962	$(7.05\ 0.18\ 0.21)\times10^{-5}$	$(1.86\ \ 0.05\ 0.05)\times10^{-4}$
$48.5 - 52.2$	1772	$(5.89\ 0.16\ 0.17)\times10^{-5}$	$(1.91\ \ 0.05\ 0.05)\times10^{-4}$
$52.2 - 56.1$	1528	$(4.82\ 0.14\ 0.14)\times10^{-5}$	$(1.91\ \ 0.06\ 0.05)\times10^{-4}$
$56.1 - 60.3$	1300	$(3.99\ 0.13\ 0.12)\times10^{-5}$	$(1.94\ \ 0.06\ 0.05)\times10^{-4}$
$60.3 - 64.8$	1143	$(3.09\ 0.11\ 0.10)\times10^{-5}$	$(1.84\ \ 0.06\ 0.06)\times10^{-4}$
$64.8 - 69.7$	1002	$(2.43\ 0.09\ 0.08)\times10^{-5}$	$(1.77\ \ 0.07\ 0.06)\times10^{-4}$
$69.7 - 74.9$	916	$(2.06\ 0.08\ 0.07)\times10^{-5}$	$(1.84\ \ 0.08\ 0.06)\times10^{-4}$
$74.9 - 80.5$	841	$(1.78\ 0.08\ 0.07)\times10^{-5}$	$(1.94\ \ 0.08\ 0.07)\times10^{-4}$
$80.5 - 93.0$	1270	$(1.22\ 0.04\ 0.05)\times10^{-5}$	$(1.80\ \ 0.07\ 0.06)\times10^{-4}$
$93.0 - 108$	980	$(7.86\ 0.35\ 0.34)\times10^{-6}$	$(1.75\ \ 0.08\ 0.07)\times10^{-4}$
$108 - 125$	733	$(5.09\ 0.29\ 0.24)\times10^{-6}$	$(1.72\ \ 0.10\ 0.08)\times10^{-4}$
$125 - 147$	573	$(3.39\ 0.24\ 0.17)\times10^{-6}$	$(1.77\ \ 0.12\ 0.08)\times10^{-4}$
$147 - 175$	223	$(2.08\ 0.20\ 0.12)\times10^{-6}$	$(1.74\ \ 0.17\ 0.10)\times10^{-4}$
$175 - 211$	83	$(1.33\ 0.19\ 0.11)\times10^{-6}$	$(1.86\ \ 0.26\ 0.15)\times10^{-4}$
$211 - 259$	72	$(9.11\ 1.42\ 0.93)\times10^{-7}$	$(2.20\ \ 0.34\ 0.22)\times10^{-4}$
$259 - 450$	66	$(2.13\ 0.51\ 0.29)\times10^{-7}$	$(1.43\ \ 0.34\ 0.19)\times10^{-4}$

TABLE SM II: The antiproton-to-positron flux ratio $\Phi^{\bar{p}}/\Phi^{e^+}$ and the antiproton-to-electron flux ratio $\Phi^{\bar{p}}/\Phi^{e^-}$ as a function of the absolute value of the rigidity at the top of AMS. σ_{stat} are the statistical errors on the ratios, σ_{syst} are the systematic errors on the ratios, and σ_{scale} are the errors from the energy scale uncertainty in $\Phi^{e^\pm}$. The antiproton flux binning is used. In the calculation of the flux ratios, $\Phi^{\bar{p}}$ and its errors are from Table I and Φ^{e^+} and Φ^{e^-} and their errors are calculated from the data used in Table I of Ref. [15].

Rigidity [GV]	$\Phi^{\bar{p}}/\Phi^{e^+}$	σ_{stat}	σ_{syst}	σ_{scale}	$\Phi^{\bar{p}}/\Phi^{e^-}$	σ_{stat}	σ_{syst}	σ_{scale}
$10.1 - 11.0$	$(3.77$	0.05	0.19	$0.23) \times 10^{-1}$	$(2.12$	0.02	0.10	$0.13) \times 10^{-2}$
$11.0 - 12.0$	$(3.97$	0.05	0.19	$0.24) \times 10^{-1}$	$(2.24$	0.02	0.11	$0.14) \times 10^{-2}$
$12.0 - 13.0$	$(4.15$	0.06	0.20	$0.22) \times 10^{-1}$	$(2.40$	0.02	0.12	$0.15) \times 10^{-2}$
$13.0 - 14.1$	$(4.50$	0.07	0.22	$0.33) \times 10^{-1}$	$(2.62$	0.02	0.12	$0.17) \times 10^{-2}$
$14.1 - 15.3$	$(4.82$	0.08	0.23	$0.26) \times 10^{-1}$	$(2.82$	0.02	0.14	$0.18) \times 10^{-2}$
$15.3 - 16.6$	$(4.78$	0.08	0.23	$0.28) \times 10^{-1}$	$(2.97$	0.03	0.14	$0.19) \times 10^{-2}$
$16.6 - 18.0$	$(4.86$	0.08	0.23	$0.29) \times 10^{-1}$	$(3.09$	0.03	0.14	$0.21) \times 10^{-2}$
$18.0 - 19.5$	$(4.92$	0.09	0.23	$0.27) \times 10^{-1}$	$(3.21$	0.03	0.15	$0.21) \times 10^{-2}$
$19.5 - 21.1$	$(5.09$	0.10	0.23	$0.35) \times 10^{-1}$	$(3.40$	0.03	0.15	$0.23) \times 10^{-2}$
$21.1 - 22.8$	$(5.35$	0.11	0.23	$0.32) \times 10^{-1}$	$(3.60$	0.04	0.16	$0.22) \times 10^{-2}$
$22.8 - 24.7$	$(5.24$	0.11	0.22	$0.27) \times 10^{-1}$	$(3.67$	0.04	0.16	$0.25) \times 10^{-2}$
$24.7 - 26.7$	$(5.52$	0.12	0.23	$0.37) \times 10^{-1}$	$(3.91$	0.04	0.16	$0.26) \times 10^{-2}$
$26.7 - 28.8$	$(5.50$	0.13	0.23	$0.25) \times 10^{-1}$	$(4.07$	0.05	0.17	$0.27) \times 10^{-2}$
$28.8 - 31.1$	$(5.46$	0.14	0.22	$0.38) \times 10^{-1}$	$(4.22$	0.05	0.17	$0.29) \times 10^{-2}$
$31.1 - 33.5$	$(5.32$	0.15	0.21	$0.30) \times 10^{-1}$	$(4.20$	0.06	0.17	$0.28) \times 10^{-2}$
$33.5 - 36.1$	$(5.65$	0.17	0.23	$0.36) \times 10^{-1}$	$(4.59$	0.07	0.18	$0.28) \times 10^{-2}$
$36.1 - 38.9$	$(5.54$	0.17	0.22	$0.21) \times 10^{-1}$	$(4.61$	0.08	0.18	$0.30) \times 10^{-2}$
$38.9 - 41.9$	$(5.19$	0.19	0.21	$0.33) \times 10^{-1}$	$(4.67$	0.11	0.19	$0.29) \times 10^{-2}$
$41.9 - 45.1$	$(5.28$	0.21	0.21	$0.19) \times 10^{-1}$	$(4.62$	0.11	0.18	$0.33) \times 10^{-2}$
$45.1 - 48.5$	$(5.18$	0.23	0.21	$0.44) \times 10^{-1}$	$(4.75$	0.13	0.19	$0.28) \times 10^{-2}$
$48.5 - 52.2$	$(5.34$	0.25	0.22	$0.23) \times 10^{-1}$	$(5.02$	0.14	0.20	$0.33) \times 10^{-2}$
$52.2 - 56.1$	$(5.20$	0.26	0.21	$0.32) \times 10^{-1}$	$(5.21$	0.16	0.21	$0.35) \times 10^{-2}$
$56.1 - 60.3$	$(5.46$	0.30	0.23	$0.27) \times 10^{-1}$	$(5.47$	0.19	0.23	$0.33) \times 10^{-2}$
$60.3 - 64.8$	$(5.07$	0.30	0.22	$0.29) \times 10^{-1}$	$(5.30$	0.20	0.23	$0.37) \times 10^{-2}$
$64.8 - 69.7$	$(4.77$	0.30	0.22	$0.18) \times 10^{-1}$	$(5.41$	0.22	0.24	$0.41) \times 10^{-2}$
$69.7 - 74.9$	$(4.81$	0.32	0.23	$0.28) \times 10^{-1}$	$(5.79$	0.26	0.27	$0.31) \times 10^{-2}$
$74.9 - 80.5$	$(5.35$	0.39	0.26	$0.44) \times 10^{-1}$	$(6.23$	0.29	0.30	$0.43) \times 10^{-2}$
$80.5 - 93.0$	$(4.41$	0.25	0.22	$0.17) \times 10^{-1}$	$(5.96$	0.24	0.30	$0.37) \times 10^{-2}$
$93.0 - 108$	$(4.73$	0.32	0.26	$0.34) \times 10^{-1}$	$(6.00$	0.29	0.32	$0.33) \times 10^{-2}$
$108 - 125$	$(4.81$	0.41	0.29	$0.28) \times 10^{-1}$	$(6.17$	0.38	0.36	$0.37) \times 10^{-2}$
$125 - 147$	$(4.96$	0.49	0.32	$0.28) \times 10^{-1}$	$(6.90$	0.51	0.42	$0.52) \times 10^{-2}$
$147 - 175$	$(4.08$	0.51	0.29	$0.23) \times 10^{-1}$	$(7.06$	0.72	0.48	$0.43) \times 10^{-2}$
$175 - 211$	$(4.71$	0.80	0.45	$0.24) \times 10^{-1}$	$(8.05$	1.16	0.74	$0.53) \times 10^{-2}$
$211 - 259$	$(5.43$	1.05	0.62	$0.31) \times 10^{-1}$	$(1.01$	0.16	0.11	$0.05) \times 10^{-1}$

(Table continued)

TABLE SM II. *(Continued)*

Rigidity [GV]	$\Phi^{\bar{p}}/\Phi^{e^+}$	σ_{stat}	σ_{syst}	σ_{scale}	$\Phi^{\bar{p}}/\Phi^{e^-}$	σ_{stat}	σ_{syst}	σ_{scale}
$259 - 450$	$(3.85$	1.05	0.58	$0.29) \times 10^{-1}$	$(7.56$	1.83	1.12	$0.59) \times 10^{-2}$

TABLE SM III: The proton-to-positron flux ratio Φ^p/Φ^{e^+} and proton-to-electron flux ratio Φ^p/Φ^{e^-} as a function of the absolute value of the rigidity at the top of AMS. σ_{stat} are the statistical errors of the flux ratios, σ_{syst} are the systematic errors of of the flux ratios, and σ_{scale} are the errors from the energy scale uncertainty of $\Phi^{e^\pm}$. The binning of the positron and electron fluxes is used [15]. In the calculation of the flux ratios, $\Phi^{e^\pm}$ and their errors are from Table I of Ref. [15] and Φ^p and its errors are calculated from the data used in Table I of Ref. [16].

Rigidity [GV]	Φ^p/Φ^{e^+}	σ_{stat}	σ_{syst}	σ_{scale}	Φ^p/Φ^{e^-}	σ_{stat}	σ_{syst}	σ_{scale}
$10.3 - 11.0$	$(2.10$	0.02	0.06	$0.13)\times10^3$	$(1.18$	0.00	0.03	$0.07)\times10^2$
$11.0 - 11.8$	$(2.15$	0.03	0.06	$0.13)\times10^3$	$(1.22$	0.00	0.03	$0.08)\times10^2$
$11.8 - 12.6$	$(2.21$	0.03	0.06	$0.12)\times10^3$	$(1.27$	0.00	0.03	$0.08)\times10^2$
$12.6 - 13.4$	$(2.22$	0.03	0.06	$0.14)\times10^3$	$(1.31$	0.00	0.04	$0.08)\times10^2$
$13.4 - 14.2$	$(2.36$	0.04	0.07	$0.16)\times10^3$	$(1.36$	0.00	0.04	$0.09)\times10^2$
$14.2 - 15.1$	$(2.41$	0.04	0.07	$0.13)\times10^3$	$(1.41$	0.00	0.04	$0.09)\times10^2$
$15.1 - 16.1$	$(2.38$	0.04	0.07	$0.13)\times10^3$	$(1.47$	0.01	0.04	$0.10)\times10^2$
$16.1 - 17.0$	$(2.41$	0.04	0.07	$0.14)\times10^3$	$(1.51$	0.01	0.04	$0.10)\times10^2$
$17.0 - 18.0$	$(2.45$	0.04	0.07	$0.15)\times10^3$	$(1.57$	0.01	0.04	$0.10)\times10^2$
$18.0 - 19.0$	$(2.49$	0.05	0.07	$0.14)\times10^3$	$(1.61$	0.01	0.04	$0.11)\times10^2$
$19.0 - 20.0$	$(2.49$	0.05	0.07	$0.15)\times10^3$	$(1.67$	0.01	0.05	$0.11)\times10^2$
$20.0 - 21.1$	$(2.59$	0.05	0.07	$0.17)\times10^3$	$(1.73$	0.01	0.05	$0.12)\times10^2$
$21.1 - 22.2$	$(2.66$	0.06	0.07	$0.16)\times10^3$	$(1.78$	0.01	0.05	$0.11)\times10^2$
$22.2 - 23.4$	$(2.69$	0.06	0.08	$0.14)\times10^3$	$(1.81$	0.01	0.05	$0.12)\times10^2$
$23.4 - 24.6$	$(2.63$	0.06	0.07	$0.15)\times10^3$	$(1.87$	0.01	0.05	$0.12)\times10^2$
$24.6 - 25.9$	$(2.71$	0.07	0.08	$0.18)\times10^3$	$(1.92$	0.01	0.05	$0.13)\times10^2$
$25.9 - 27.2$	$(2.80$	0.07	0.08	$0.15)\times10^3$	$(1.97$	0.01	0.05	$0.13)\times10^2$
$27.2 - 28.7$	$(2.72$	0.07	0.08	$0.13)\times10^3$	$(2.03$	0.01	0.06	$0.13)\times10^2$
$28.7 - 30.2$	$(2.69$	0.07	0.08	$0.17)\times10^3$	$(2.07$	0.01	0.06	$0.14)\times10^2$
$30.2 - 31.8$	$(2.80$	0.08	0.08	$0.17)\times10^3$	$(2.15$	0.02	0.06	$0.15)\times10^2$
$31.8 - 33.5$	$(2.78$	0.08	0.08	$0.16)\times10^3$	$(2.21$	0.02	0.06	$0.15)\times10^2$
$33.5 - 35.4$	$(2.83$	0.09	0.08	$0.18)\times10^3$	$(2.30$	0.02	0.07	$0.15)\times10^2$
$35.4 - 37.3$	$(2.89$	0.09	0.09	$0.15)\times10^3$	$(2.31$	0.02	0.07	$0.14)\times10^2$
$37.3 - 39.4$	$(2.75$	0.09	0.08	$0.12)\times10^3$	$(2.37$	0.02	0.07	$0.16)\times10^2$
$39.4 - 41.6$	$(2.72$	0.09	0.08	$0.18)\times10^3$	$(2.46$	0.02	0.07	$0.15)\times10^2$
$41.6 - 44.0$	$(2.89$	0.11	0.09	$0.15)\times10^3$	$(2.45$	0.02	0.07	$0.16)\times10^2$
$44.0 - 46.6$	$(2.70$	0.10	0.08	$0.16)\times10^3$	$(2.58$	0.03	0.08	$0.17)\times10^2$
$46.6 - 49.3$	$(2.93$	0.12	0.09	$0.18)\times10^3$	$(2.60$	0.03	0.08	$0.16)\times10^2$
$49.3 - 52.3$	$(2.81$	0.12	0.09	$0.13)\times10^3$	$(2.68$	0.03	0.08	$0.18)\times10^2$
$52.3 - 55.6$	$(2.75$	0.12	0.09	$0.16)\times10^3$	$(2.75$	0.04	0.08	$0.18)\times10^2$
$55.6 - 59.1$	$(2.87$	0.14	0.09	$0.17)\times10^3$	$(2.85$	0.04	0.09	$0.18)\times10^2$
$59.1 - 63.0$	$(2.78$	0.14	0.09	$0.15)\times10^3$	$(2.88$	0.04	0.09	$0.19)\times10^2$
$63.0 - 67.3$	$(2.81$	0.15	0.09	$0.13)\times10^3$	$(3.01$	0.05	0.09	$0.22)\times10^2$

(Table continued)

8

TABLE SM III. *(Continued)*

| Rigidity [GV]	Φ^p/Φ^{e^+}	σ_{stat}	σ_{syst}	σ_{scale}	Φ^p/Φ^{e^-}	σ_{stat}	σ_{syst}	σ_{scale}
$67.3 - 72.0$	(2.64	0.14	0.09	$0.13)\times10^3$	(3.21	0.05	0.10	$0.21)\times10^2$
$72.0 - 77.4$	(2.66	0.15	0.09	$0.19)\times10^3$	(3.17	0.06	0.10	$0.19)\times10^2$
$77.4 - 83.4$	(2.92	0.17	0.10	$0.13)\times10^3$	(3.31	0.06	0.11	$0.21)\times10^2$
$83.4 - 90.2$	(2.45	0.14	0.08	$0.10)\times10^3$	(3.33	0.07	0.11	$0.21)\times10^2$
$90.2 - 98.1$	(2.60	0.16	0.09	$0.18)\times10^3$	(3.46	0.07	0.12	$0.21)\times10^2$
$98.1 - 107$	(2.78	0.19	0.11	$0.18)\times10^3$	(3.45	0.08	0.13	$0.21)\times10^2$
$107 - 118$	(2.80	0.20	0.12	$0.16)\times10^3$	(3.58	0.08	0.13	$0.23)\times10^2$
$118 - 132$	(2.83	0.22	0.12	$0.16)\times10^3$	(3.68	0.09	0.14	$0.25)\times10^2$
$132 - 149$	(2.82	0.24	0.12	$0.12)\times10^3$	(4.05	0.12	0.16	$0.27)\times10^2$
$149 - 170$	(2.35	0.20	0.10	$0.12)\times10^3$	(4.07	0.13	0.16	$0.24)\times10^2$
$170 - 198$	(2.58	0.26	0.12	$0.16)\times10^3$	(4.27	0.15	0.17	$0.28)\times10^2$
$198 - 237$	(2.47	0.28	0.13	$0.13)\times10^3$	(4.62	0.18	0.21	$0.28)\times10^2$
$237 - 290$	(2.49	0.35	0.15	$0.15)\times10^3$	(4.54	0.21	0.23	$0.27)\times10^2$
$290 - 370$	(2.61	0.51	0.17	$0.18)\times10^3$	(5.11	0.30	0.32	$0.39)\times10^2$
$370 - 500$	(3.07	0.91	0.28	$0.32)\times10^3$	(6.26	0.53	0.48	$0.60)\times10^2$
$500 - 700$					(7.11	1.01	1.12	$0.85)\times10^2$
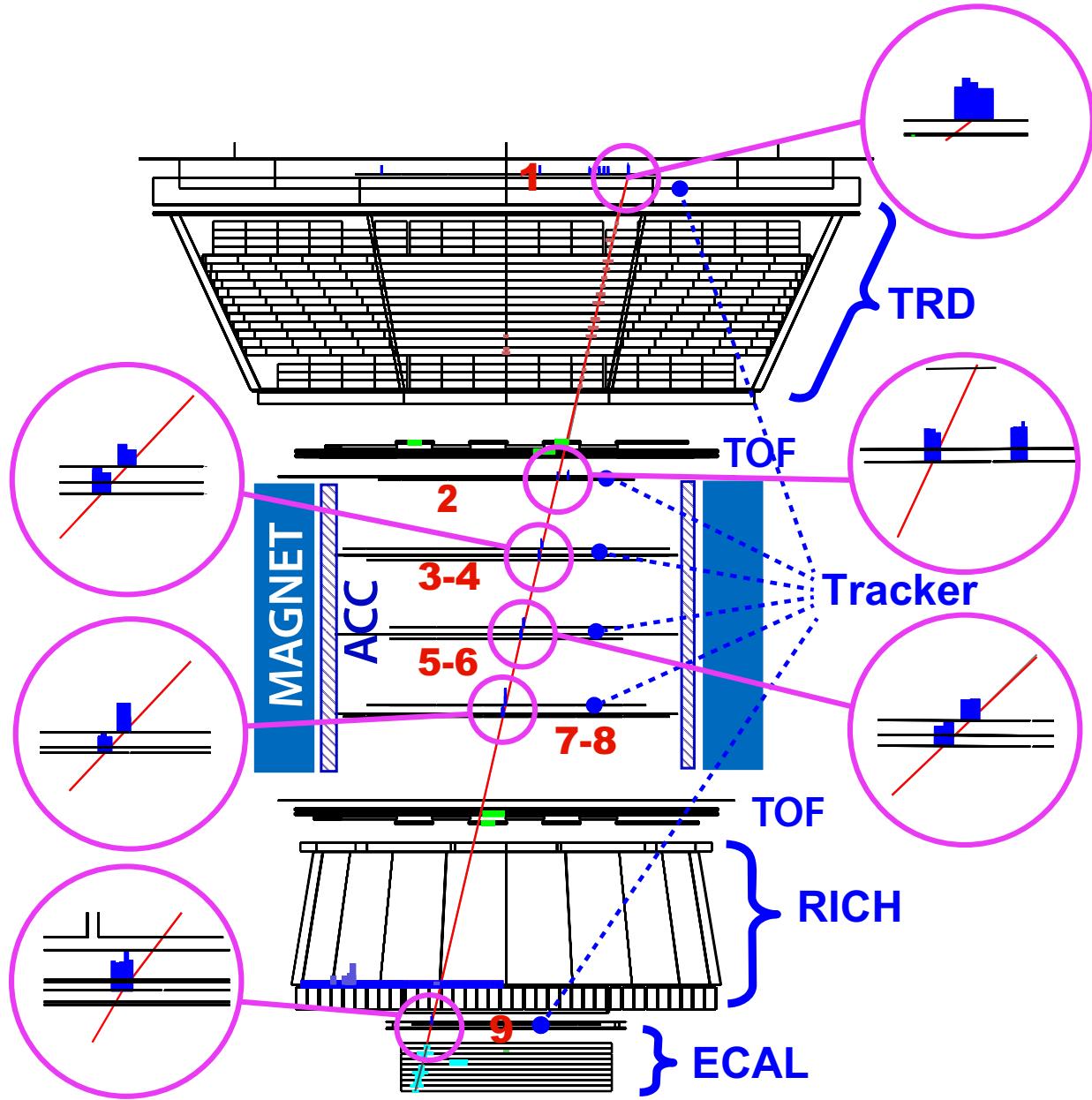
FIG. SM 1. An event display in the bending plane of an antiproton. The red line indicates the reconstructed trajectory or track. The insets indicate the matching of the track to the pulse heights measured in each layer of the tracker. This downward-going $|Z| = 1$ event is identified as an antiproton with $R = -435$ GV, $\Lambda_{\mathrm{TRD}} = 0.908$, and $\Lambda_{\mathrm{CC}} = 0.983$.
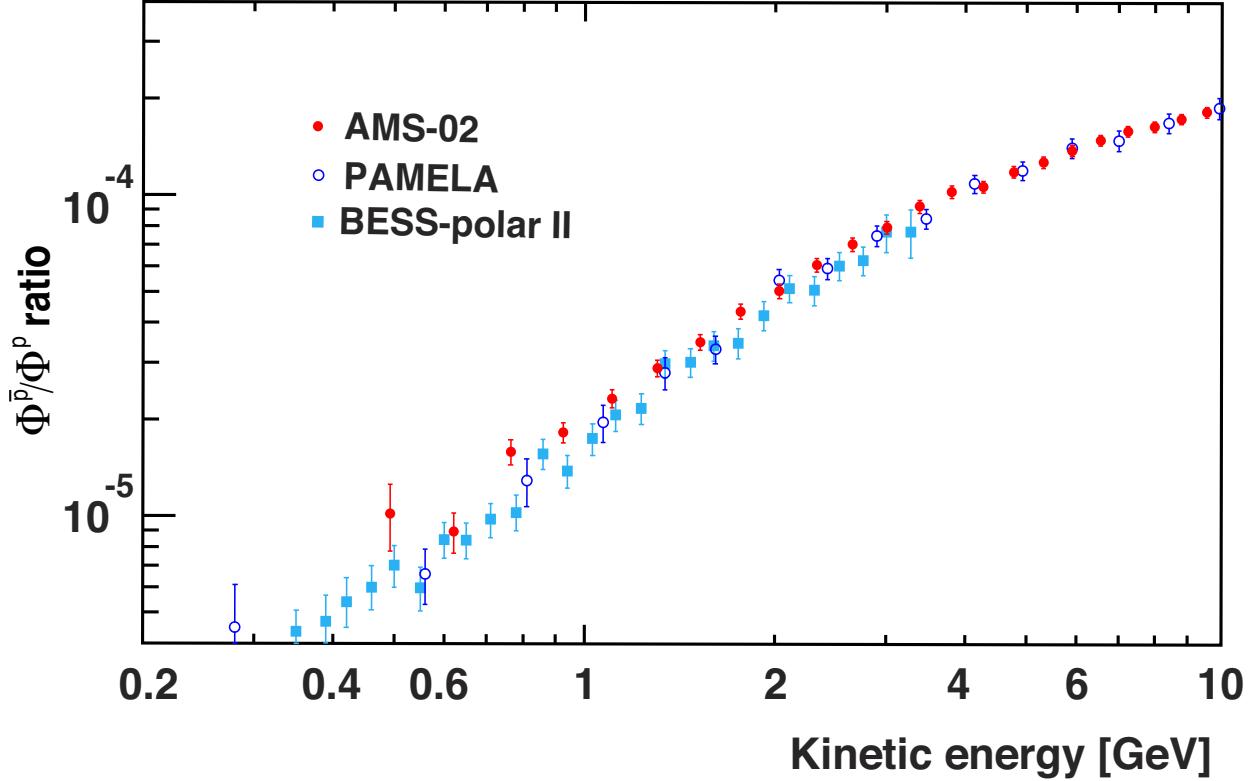
FIG. SM 2. The measured $(\bar{p}/p)$ flux ratio as a function of the kinetic energy up to 10 GeV. The kinetic energy is defined as $E_K = \sqrt{R^2 + M^2} - M$ where M is the antiproton or proton mass. The BESS [2] and PAMELA [6] measurements are also shown. For the AMS data, the error bars are the quadratic sum of statistical and systematic errors. Horizontally, the data points are placed at the center of each bin.
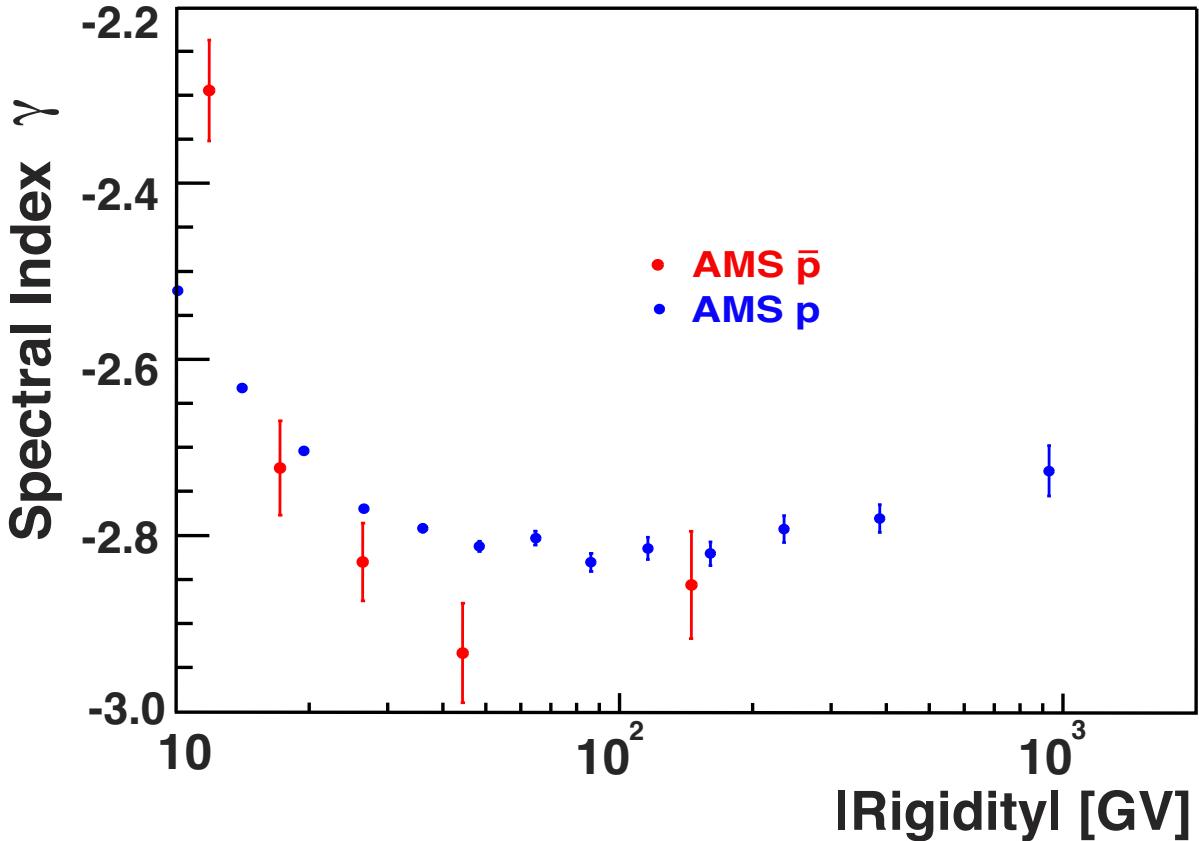
FIG. SM 3. The spectral index vs $|R|$ of the antiproton flux (red), where the highest rigidity antiproton point corresponds to $60.3 \leq |R| < 450$ GV, compared with the proton flux spectral index (blue) [16]. The spectral index for antiprotons with $60.3 \leq |R| < 450$ GV is consistent with the proton spectral index. The error bars correspond to the quadratic sum of the statistical and uncorrelated systematic errors. Horizontally, the points are placed at $\hat{R}$.
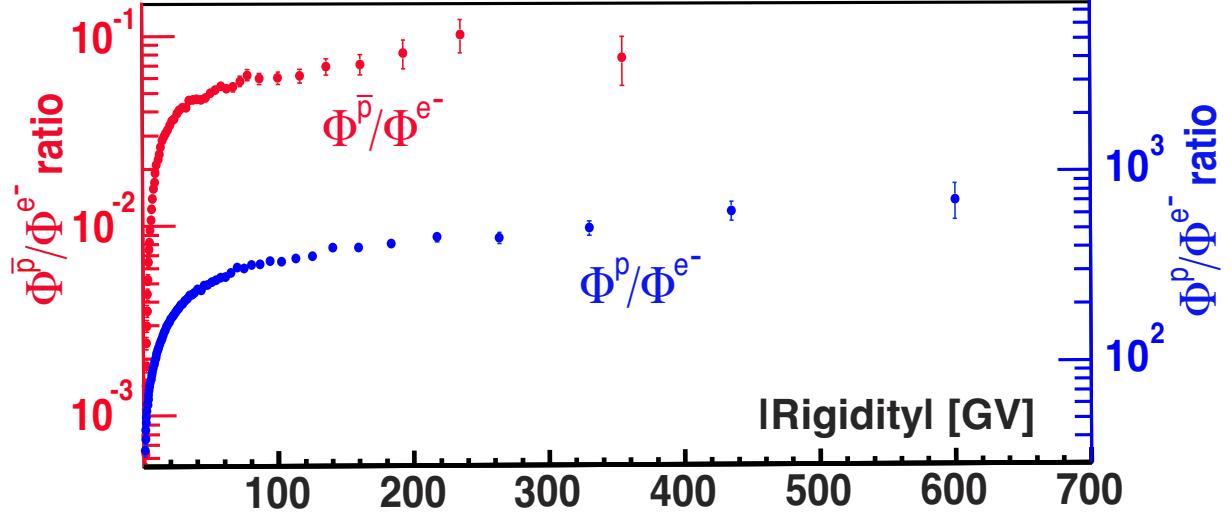
FIG. SM 4. The measured $(\bar{p}/e^-)$ (red, left axis) and (p/e^-) (blue, right axis) flux ratios as a function of the absolute value of the rigidity. Note that the (p/e^-) flux ratio also extends to higher rigidity than the $(\bar{p}/e^-)$ flux ratio and has smaller errors. The error bars are the quadratic sum of statistical and systematic errors. Horizontally, the data points are placed at the center of each bin.
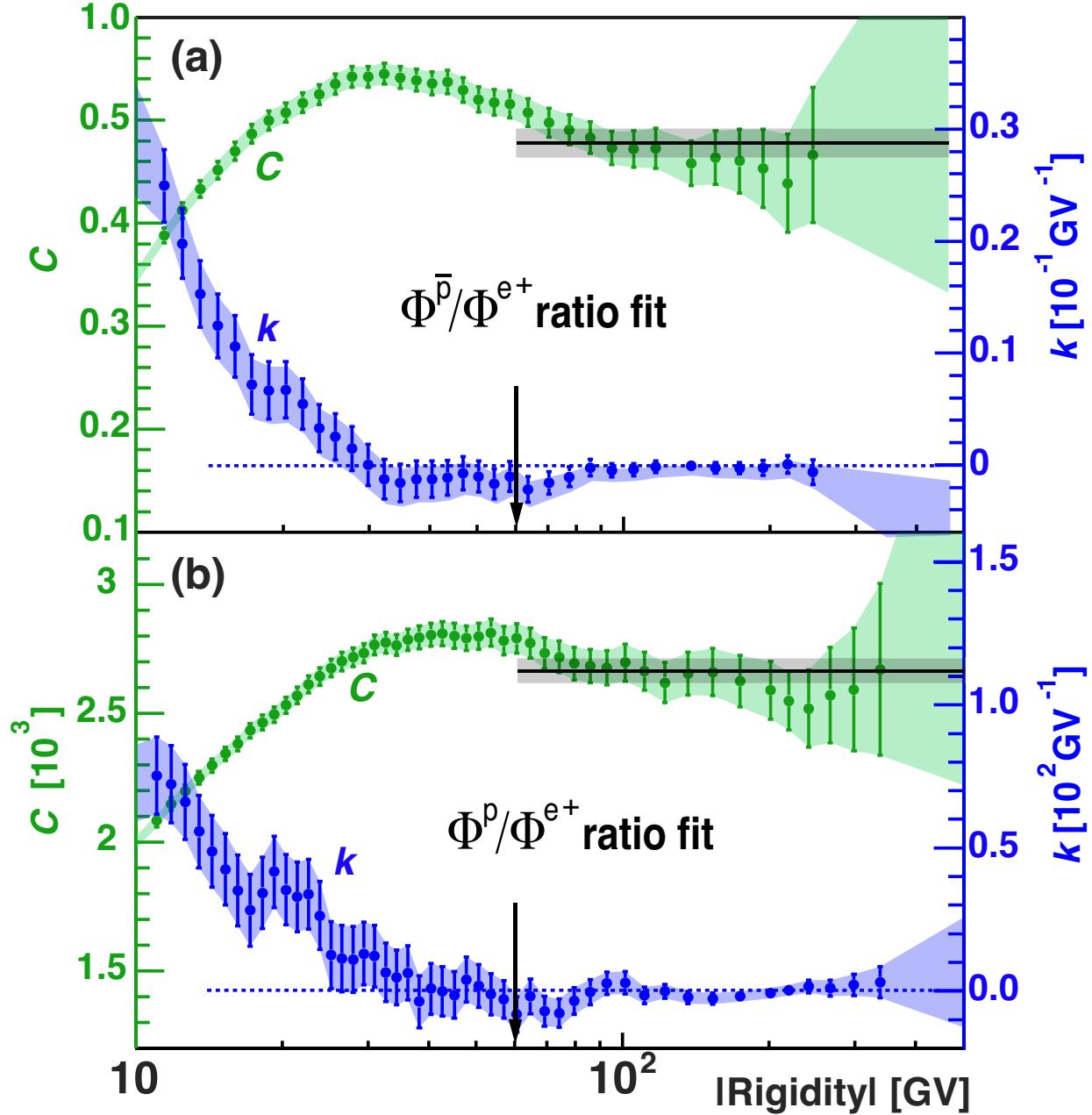
FIG. SM 5. Sliding window fits of Eq. (4) to the (a) ($\bar{p}/e^+$) and (b) (p/e^+) flux ratios measured by AMS with parameter C (green, left axis) and the slope k (blue, right axis). The green and blue shaded regions indicate that the errors are correlated between adjacent points. The points are placed at R_0. The dashed blue lines at $k = 0$ are to guide the eye. The black arrows indicate the lowest rigidities above which the flux ratios are consistent with being rigidity independent and the black horizontal bands show the mean values and the 1-sigma errors of the flux ratios above this rigidity.